

Degradation Mechanism Induced by Depth-Dependent Inhomogeneity in Thick High-Areal-Capacity Graphite Electrode

Kun-Hee Ko, Kyoungoh Kim, Youngsu Kim, Sangwook Han, Jooha Park, Hayoung Park, Jaedong Yang, Beomkwon Kim, Jungwon Park, and Kisuk Kang*

Employing thick electrodes with high active material loading is one of the most practical approaches to enhance the energy density of lithium-ion batteries by fully leverage the potential of electrode materials. However, use of thick electrodes typically leads to a significant decline in electrode performance, accompanied by accelerated electrode degradation. Herein, the degradation mechanism is elucidated in high-loading graphite electrodes, driven by depthdependent reaction inhomogeneity along the electrode thickness. It is demonstrated that the inhomogeneity is primarily caused by entrapment of lithium ions at the bottom of the electrode, progressively worsening with cycles, and contributes to the generation of current hotspots particularly at the top of the electrode. These hotspots trigger excessive solid electrolyte interphase formation, causing a sharp rise in charge transfer resistance and further exacerbating reaction inhomogeneity. It is further shown that the protection of the electrode surface mitigates the side reactions induced by current hotspots, breaking the negative feedback loop between electrode resistance and reaction inhomogeneity. The negative feedback loop in the degradation mechanism suggests a need for a comprehensive strategy that not only enhances diffusion process commonly targeted for improving thick electrode performance but mitigates the surface reaction for the successful implementation of high-loading electrodes.

1. Introduction

To meet the growing demands for longer driving ranges at lower costs in the electric vehicle market, extensive research efforts

are underway to enhance the energy density and to reduce the cost of lithium-ion batteries.[1-4] Despite significant advancements in lithium-ion battery technology, particularly with advanced layered oxide cathodes and graphite anodes, the market continues to push for batteries with even higher energy densities. Consequently, researches have been conducted to break through the limitations of current lithiumion battery systems by developing new highcapacity active materials, such as lithium metal/alloy,[5-7] silicon based anodes,[8-14] and high-nickel[15-17] or lithium-rich layered oxide[18-20] cathodes. While ongoing exploration of these new active materials continues, the progress in energy density increase remains staggering and still falls short of the demanding requirements for next-generation electric vehicles. Furthermore, although these novel electrode materials are anticipated to improve the performance of existing lithium-ion batteries, the practical integration of new chemistries

poses additional challenges for reconfiguring battery manufacturing processes.

An alternative approach to enhancing energy density involves optimizing the design of battery to minimize the use of

K.-H. Ko, K. Kim, Y. Kim, S. Han, J. Park, K. Kang Department of Materials Science and Engineering Institute for Rechargeable Battery Innovations Research Institute of Advanced Materials Seoul National University 1 Gwanak-ro, Gwanak-gu, Seoul 08826, Republic of Korea E-mail: matlgen1@snu.ac.kr

The ORCID identification number(s) for the author(s) of this article can be found under https://doi.org/10.1002/smll.202410795

[+] Present address: Department of Chemical and Biomolecular Engineering, University of California, Los Angeles, Los Angeles, CA 90095,

© 2025 The Author(s). Small published by Wiley-VCH GmbH. This is an open access article under the terms of the Creative Commons Attribution-NonCommercial-NoDerivs License, which permits use and distribution in any medium, provided the original work is properly cited, the use is non-commercial and no modifications or adaptations are made.

DOI: 10.1002/smll.202410795

H. Park^[+], J. Park
School of Chemical and Biological Engineering
Seoul National University
1 Gwanak-ro, Gwanak-gu, Seoul 08826, Republic of Korea
H. Park^[+], J. Park, K. Kang
Center for Nanoparticle Research
Institute of Basic Science
Seoul National University
1 Gwanak-ro, Gwanak-gu, Seoul 08826, Republic of Korea
K. Kang

Institute of Engineering Research
College of Engineering
Seoul National University
1 Gwanak-ro, Gwanak-gu, Seoul 08826, Republic of Korea
J. Yang, B. Kim
SDI R&D Center
Samsung SDI Co., LTD

130 Samsung-ro, Yeongtong-gu, Suwon, Gyeonggi-do 16678, Republic of Korea

16136829, 2025, 16, Downloaded from https

//onlinelibrary.wiley.com/doi/10.1002/smll.202410795 by Korea Institute Of Science, Wiley Online Library on [01/06/2025]. See the Terms

and-conditions) on Wiley Online Library for rules of use; OA articles are governed by the applicable Creative Commons

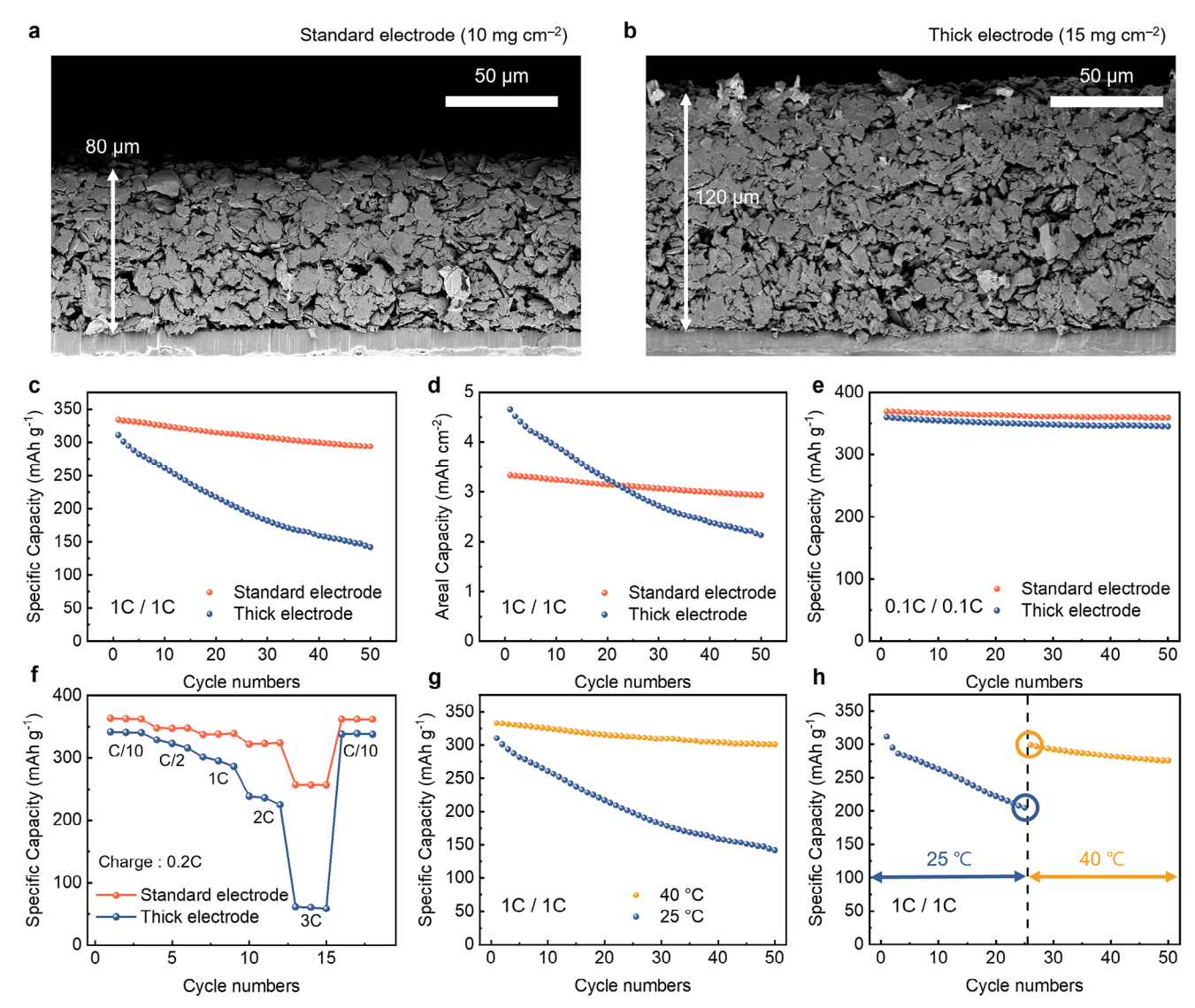


Figure 1. Comparison between standard and thick graphite electrodes. a,b) Cross-sectional SEM images of a) standard and b) thick electrodes. Comparison of cycle life of standard (orange) and thick (blue) electrodes in terms of c) specific capacity and d) areal capacity. Cycling of the cells was conducted using a 1C constant current discharge (lithiation) coupled with a constant voltage set at 0.005 V until the current rate was reduced to 0.1C. Subsequently, the cells were charged (delithiation) to a voltage threshold of 1.6 V (vs Li/Li⁺). Electrochemical performance of standard (orange) and thick electrodes (blue), showing e) cycle life at a current rate of 0.1C and f) rate capability tests. g) Cycle life of thick electrode at temperature of 25 °C (blue) and 40 °C (gold) with current rate of 1C. h) Specific capacity of the cell in which temperature is changed from 25 °C (blue) to 40 °C (gold) after 25 cycles.

inactive components that increase the weight of overall system (e.g., the current collector, separator, and packaging). [21] Over the past decade, the industrial sectors have extensively explored approaches that reduce inactive components in batteries, such as utilizing thinner current collectors and separators or employing cell-to-pack technology [22-25] to simplify battery packaging. These measures have decreased the proportion of inactive components in battery packs from over 55% in the 2010s to 40% in 2021. [26-28] Nevertheless, these attempts of partially eliminating inactive parts are currently approaching their limits arising from increased processing costs and safety concern. [29,30] Another viable strategy is to increase the mass-loading of active materials in electrode relative to inactive components, [31-36] thereby lowering the effective proportion of inactive components. As depicted

in Figure S1 (Supporting Information), an increase in the electrode mass loading by 50% can yield $\approx 16\%$ enhancement in the actual energy density of the battery using the same amount of inactive components. Despite this straightforward estimation, the adoption of high-loading electrodes is not trivial, since the thickening process accompanies the loss of electrochemical performance such as lower active material utilization and poor rate capability, as previously reported. These losses are often attributed to sluggish mass transport within electrode due to increased path length and tortuosity for electron and ion movement. Mass transport limitations observed in high-mass-loading electrodes are particularly detrimental to anode materials not only with respect to the performance but also concerning the safety. Specifically, such limitations in graphite



SMQ

www.small-journal.com

electrodes can lead to lithium metal plating due to insufficient lithium insertion kinetics and the accumulation of dead lithium, causing a short-circuit-induced safety hazard. [43-45] These conditions are analogous to those observed during fast charging at low temperatures, which has been a critical factor in the occurrence of battery fire, even in conventional graphite electrodes. [46-48]

In this study, we experimentally verify that the thick electrodes, prone to the mass transport limitations, are susceptible to rapid capacity fading because of a negative feedback loop concerning the depth-dependent lithium inhomogeneity and the local hot spots that induce side reactions. By comparatively examining electrodes with various loading levels, it is demonstrated that lithium entrapment at the bottom of the electrode initiates this reaction inhomogeneity, which progressively worsens with cycling. Moreover, it results in the formation of current hotspots, particularly at the top of the electrode, which trigger excessive SEI formation. These processes, in turn, causes a sharp increase in charge transfer resistance, further aggravating reaction inhomogeneity and ultimately leading to rapid capacity loss. Based on this observation, we also show that protecting the top electrode surface mitigates the side reactions caused by these hotspots, breaking the feedback loop between increased charge transfer resistance and reaction inhomogeneity. These findings suggest that a comprehensive approach is necessary in the implementation of highloading electrodes—one that not only targets diffusion process enhancements, which are commonly aimed at improving thick electrode performance, but also effectively manages surface side reactions.

2. Results

2.1. Electrode Mass Loading on Electrochemical Performance

In order to understand the effect of high-loading conditions on electrode performance, we first prepared a standard electrode with a mass loading of 10 mg cm⁻² using graphite as the active material. The typical loading for graphite anodes in commercial lithium-ion batteries is \approx 6 to 10 mg cm⁻² based on singlesided coating,[49-51] thus this serves as a baseline for comparison. A high-areal-capacity electrode was then fabricated with a 50% higher mass loading than the standard electrode, that is, 15 mg cm⁻², and will be referred as the "thick electrode" hereafter. Throughout the electrode fabrication process, we ensured that the densities of both electrodes remained within the same range of 1.3-1.4 mg cm⁻³ to prevent any confounding effects from differences in porosity or electrical connectivity, isolating thickness as the primary variable in our comparative evaluation. Figure 1a,b illustrate the cross-sectional images of the standard and thick electrodes, with thicknesses of 80 μm and 120 μm , respectively. Given the 50% higher mass loading of the thick electrode, the proportional relationship between mass loading and thickness confirms that both configurations have nearly identical electrode densities and porosities (See Table S1, Supporting Information for details). Each electrode was assembled into a cointype cell and cycled under a common battery operation condition, using a discharge (i.e., lithiation) rate of 1C and a charge (i.e., de-lithiation) rate of 1C, to assess electrochemical performance in Figure 1c,d. In the initial cycle, the standard and thick electrodes exhibited comparable specific discharge capacities of 333 and 310 mAh g⁻¹ (Figure S2, Supporting Information), respectively, consistent with typical commercial graphite electrode performance. [52–54] The thick electrode delivered an areal capacity of 4.66 mAh cm⁻², ≈40% higher than the standard electrode (3.34 mAh cm⁻²). This comparable discharge capacity during the initial cycle indicates that graphite utilization was not significantly hindered, even under the high-loading thick electrode condition that is expected to cause a higher charge transfer resistance. However, in continued cycling tests, the thick electrode experienced a much more rapid capacity decline than the standard electrode. After \approx 20 cycles, its areal capacity dropped even below that of the standard electrode, suggesting additional degradation mechanisms are at play under high-loading conditions, beyond simple resistance effects. To explore this further, we prepared an electrode with a 5 mg cm⁻² loading and compared its performance to the standard electrode, as shown in Figure \$3 (Supporting Information). However, the results revealed no significant difference between the two, indicating that drastic performance degradation emerges once a critical thickness threshold is surpassed.

2.2. Kinetics-Induced Performance Deterioration in Thick Electrode

To elucidate the accelerated degradation of the thick electrode, we repeated our experiment at a low current density of 0.1C, as demonstrated in Figure 1e, Figures S4 and S5 (Supporting Information). In contrast to results of 1C, both electrodes exhibited comparable capacity retention over cycles, with nearly identical initial discharge capacities. By 50 cycles, the standard and thick electrodes retained 97% and 96% of their capacity, respectively. It suggests that the inferior cycle stability of the thick electrode in Figure 1c,d is a result of kinetics-induced degradation that worsens at high current densities due to limited mass transport and charge transfer. Furthermore, the rapid rise in average delithiation voltage in the thick electrode reaffirms the presence of kinetic limitations (Figure S6, Supporting Information). Indeed, differences in rate capability were apparent between the two electrodes as shown in Figure 1f. At a current rate of 3C, the standard electrode retains 70% of its capacity relative to 0.1C, whereas the thick electrode sustained only 18%. High-temperature electrochemical tests further verify that kinetic limitations are a key factor limiting the cycle stability of thick electrodes. As depicted in Figure 1g, the rapid capacity decay observed in the thick electrode at room temperature (denoted with blue line) is significantly mitigated at 40 °C (denoted with yellow line), where kinetic hindrance is reduced. Moreover, switching the temperature from room temperature to 40 °C could recover the capacity lost during cycles, as presented in Figures 1h and S7 (Supporting Information). In specific, the capacity drops to $\approx 180 \text{ mAh g}^{-1}$ at 1C after 25 cycles at room temperature, but when the temperature is raised to 40 °C in a continued cycle test, the capacity recovers to ≈ 300 mAh g⁻¹, indicating that the capacity loss is not the result of irreversible damages of the graphite electrode but comes from the kinetical hindrance that grows over cycles.

To understand the origin of the kinetics-induced degradation in thick electrodes, we systematically analyzed the conditions of each electrode over cycles, particularly focusing on the effect of an elongated charge carrier path along the thick electrode. [34]



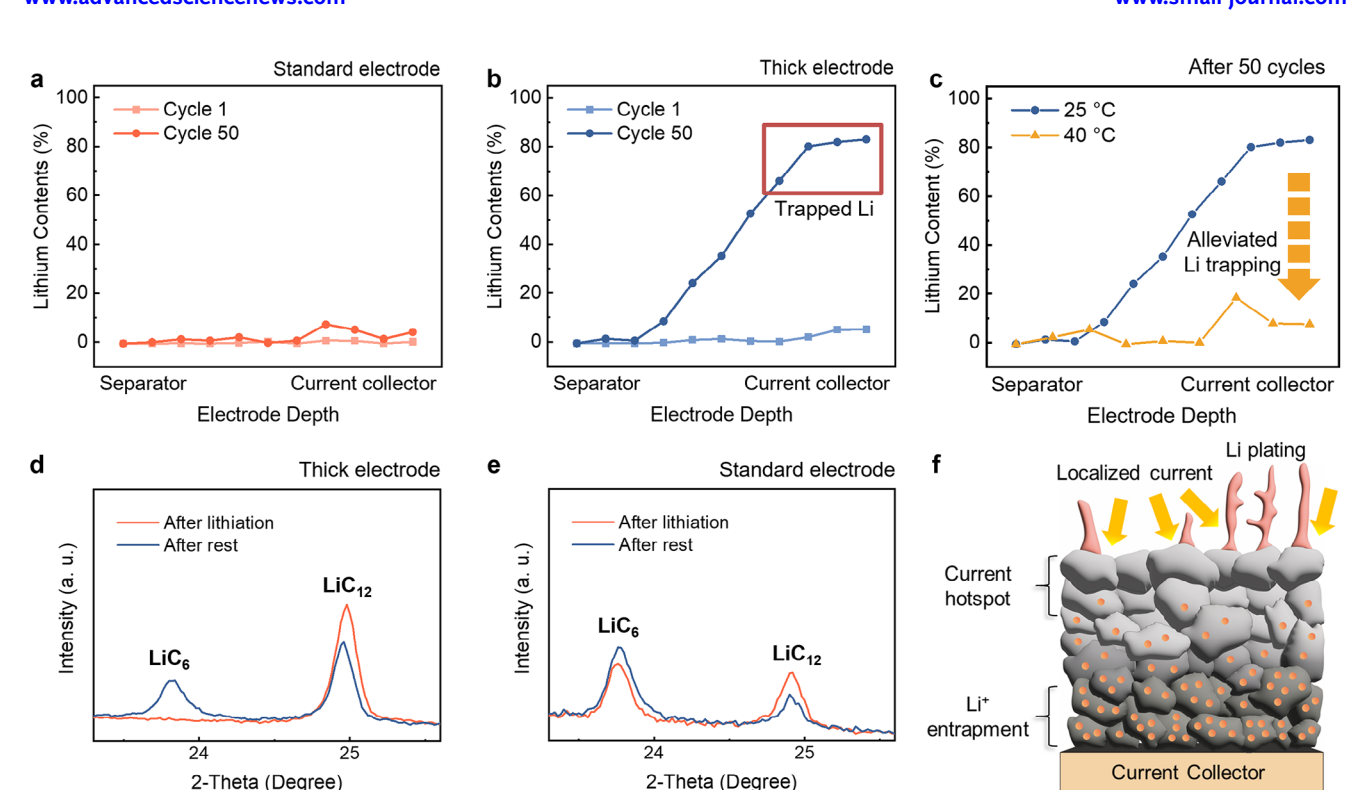


Figure 2. Observation of reaction inhomogeneity along the electrode depth and its consequences. a,b) Laser induced breakdown spectroscopy (LIBS) analysis depicting the initial (light color) and fiftieth (dark color) cycle for a) the standard electrode and b) the thick electrode at room temperature. c) the lithium content comparison in the thick electrode after 50 cycles at the temperature of 25 °C (blue) and 40 °C (gold). d,e) X-ray diffraction result of d) thick and e) standard electrode immediately after lithiation (orange) and after 16 h of rest (blue). f) Schematic illustration showing the heterogeneity in the graphite thick electrode and subsequent effects.

The spatial distribution of reactions was monitored by quantitatively measuring lithium content (i.e., state of charge (SOC)) using the laser-induced breakdown spectroscopy (LIBS) with depth profiling. [34,55] In our experiment, the LIBS energy level was calibrated to allow depth profiling on a micrometer scale, enabling profiling for both standard and thick electrodes. A depth equivalent to 10% of the electrode thickness was probed per measurement shot with total ten measurements for the entire electrode. (See experimental section for the details of LIBS measurement). LIBS analysis revealed that the thick electrode exhibits significant reaction inhomogeneity along its depth. Figure 2a,b illustrate the lithium content distribution for standard and thick electrodes after the first and fiftieth cycle, from the top layer (separator side) to the bottom layer (current collector side). In the standard electrode, lithium distribution is uniform across the electrode depth, with nearly complete extraction during de-lithiation after the initial cycle. Even after 50 cycles, the lithium distribution remains homogeneous, with only minimal lithium entrapment near the current collector (Figure 2a), indicating reactions occur homogenously throughout the electrode. In the thick electrode, however, significant deviations in lithium composition are observed along the depth from the current collector to the separator side, which becomes more pronounced with cycling. As illustrated in Figure 2b, while lithium distribution is relatively uniform after the first cycle, it becomes highly heterogeneous after 50 cycles, with substantial lithium remaining trapped even after full charge up to 1.6 V

(vs Li/Li+). Notably, the bottom 30% of the electrode (current collector side) contains a high concentration of lithium, with over 80% of lithium remaining unextracted, suggesting that the de-lithiation is predominantly localized in the top layers. This localized top-layer reaction far from the current collector implies that the lithium-ion mobility is the limiting factor in the charge balance between the electronic and ionic transport in the electrode reaction, as similarly reported in the cathode composites in solid-state batteries. [56–58] Further analysis of lithium distribution at elevated temperatures also confirms that the reaction inhomogeneity is primarily due to slow lithium diffusion. Figure 2c compares lithium contents of thick electrode after 50 cycles at 25 °C and those at 40 °C. It shows there is a considerable reduction in trapped lithium throughout the electrode when operated at an elevated temperature. In the top 70% of the electrode thickness (from the separator side), the majority of lithium was able to be de-intercalated during de-lithiation process. Even near the current collector, only $\approx 10\%$ of lithium remains trapped, a significant improvement from the 80% entrapment observed at room temperature. These evidences suggest that limited lithium-ion diffusion kinetics are primarily responsible for the inhomogeneous reaction behavior in thick graphite electrodes.

We supposed that the inhomogeneous reaction with less active bottom electrode part would lead to an effectively high current density locally concentrated on the top layer of the electrode. During re-lithiation, this elevated current density would cause

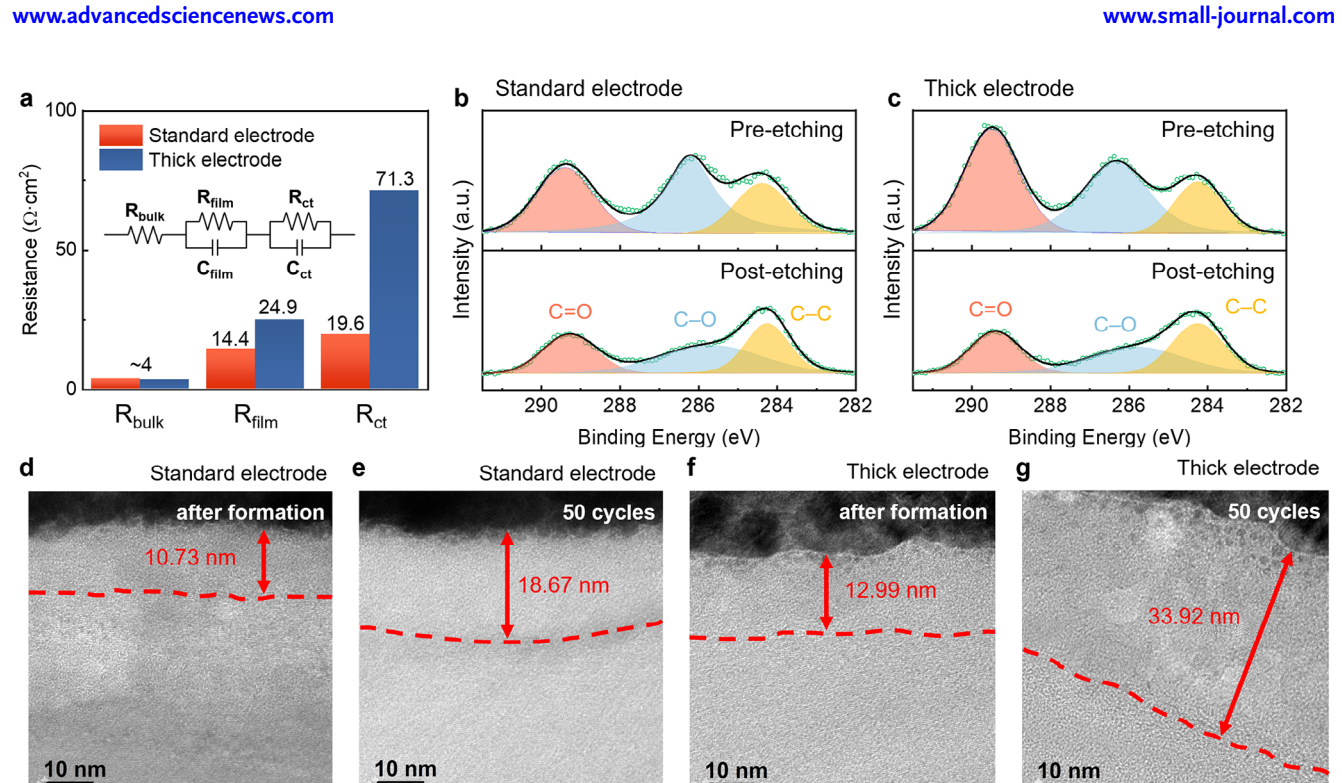


Figure 3. Surface degradation characterization of graphite electrodes. a) Electrochemical impedance spectroscopy (EIS) result of standard (orange) and thick (blue) electrode. b,c) X-ray Photoelectron Spectroscopy (XPS) results for both pre-etching (top) and post-etching (bottom) phases for b) standard and c) thick electrodes, with spectra deconvoluted into peaks for C-C (yellow; 284.3 eV), C-O (blue; 286.3 eV), and C-O (red; 289.3 eV). d-g) Cryogenic transmission electron microscopy (Cryo-TEM) results for the standard (d: after formation cycle, e: after 50 cycles) and thick electrodes (f: after formation cycle, g: after 50 cycles).

significant overpotentials, as commonly reported in studies on fast charging or low-temperature operation, driving the anode potential below 0 V and leading to lithium plating.[59-64] Considering direct observation of local lithium formation would be challenging, we attempted to probe the possible overpotential-driven lithium plating through changes in the graphite lithiation state in electrodes, inferred from time-dependent XRD peak evolution. The idea was based on that the instant overpotential-driven heterogeneity would gradually disappear during relaxation period, recovering the near-equilibrium state. For example, lithium plated on the carbon electrode surface would spontaneously intercalate into the graphite during the rest period, causing the change in the lithiation state of graphite. [65-67] Figure 2d,e comparatively illustrate the evolution of XRD peaks of the thick and standard graphite electrodes, which were recorded during 16-hour resting period after electrochemical lithiation. The thick electrode in Figure 2d indicates the graphite forming LiC₁₂ as a main phase immediately after the electrochemical lithiation. This appears to be inconsistent with the amount of specific capacity measured during lithiation (310 mAh g⁻¹, see electrochemical profile of Figure S2, Supporting Information), which corresponds to the formation of mixed LiC₆ and LiC₁₂ phases. However, upon resting for 16 h, a significant reduction in the LiC₁₂ peak intensity is observed alongside an increase in the LiC6 peak intensity, indicating a dynamic shift in the lithiation states within the electrode over time. It strongly suggests that chemical lithiation has taken place during this period, converting LiC₁₂ to LiC₆, which would be only possible with a lower-reduction-potential mate-

rial present in the electrode, that is, lithium metal. In contrast, XRD peak intensities of LiC₆ and LiC₁₂ show minimal changes in the standard electrode between measurements taken right after lithiation and those after resting (Figure 2e). The apparent difference in dynamic change in lithiation state of graphite evidences the local lithium plating in the thick graphite electrode. The observed reaction inhomogeneity and lithium plating propose that thick electrodes are likely to degrade through mechanisms distinct from those in standard electrodes, as summarized in Figure 2f. The extended paths for charge carriers within the thick electrode result in non-uniform electrochemical reactions across the electrode depth, causing lithium ions to accumulate in lower layers near the current collector. With repeated cycles, this entrapment intensifies, and localized high current density on the top layer exacerbates reaction inhomogeneity, promoting lithium metal plating.

2.3. Electrode Surface Degradation Arising from Reaction Inhomogeneity

The local lithium metal plating on the top graphite layer would accompany subsequent side reactions with electrolyte, deteriorating the electrode surface. [68,69] According to the electrochemical impedance spectroscopy (EIS) results in Figure 3a, the impedance increase of the thick electrode was found to be significantly large than the standard electrode after cycles, supporting our speculation. [70,71] While the bulk resistance (Rbulk) was



SMQ

www.small-journal.com

similar for both electrodes, the film resistance (R_{film}) and the charge transfer resistance (R_{ct}) became considerably higher in the thick electrode after cycles (See Figure S8, Supporting Information for Nyquist plot data). Motivated by these findings, we further conducted surface analysis using X-ray photoelectron spectroscopy (XPS) for the two electrodes in Figure 3b,c. Considering the presence of common byproducts in the surface film (e.g., ROCO₂Li and Li₂CO₃), the surface degradation was estimated by comparing the amount of these components in each electrode for pre- and post-etching states. Deconvoluted peaks observed at 289.3, 286.3, and 284.3 eV in C 1s spectra are indicative of C=O, C-O, and C-C bonding structures, respectively. The peak at 284.3 eV, representing C—C bonding, is generally recognized as a fingerprint of graphite, while C=O and C-O peaks are attributed to byproducts from the decomposition of the electrolyte.^[72–75] Comparison of the pre-etching XPS spectra suggests that the peak areas for C=O and C-O bonds are substantially greater in the thick electrode. While the quantitative comparison should be done with more care, the identical post-etching signals for both qualitatively infer that the surface of the cycled thick electrode (pre-etching) contains higher contents of byproducts with C=O and C-O bondings. As detailed in Table S2 (Supporting Information), the peak areas of C=O and C-O are \approx 25% larger in the thick electrode, implying that it has suffered from more severe electrolyte decomposition than the standard electrode. The formation of an excessive SEI layer could be visually verified through cryogenic transmission electron microscopy (Cryo-TEM) analysis. TEM images in Figure 3d-g present the surface conditions of standard and thick electrodes after the formation cycle and fiftieth cycles, respectively. Initially, the SEI layer thicknesses were comparable between the two electrodes (Figure 3d,f), indicating the similar level of SEI layer formation during the formation cycle. However, after 50 cycles, the increase in SEI layer thickness was more pronounced for the thick electrode: in the standard electrode, it increased by 73% from 10.73 to 18.67 nm, and in the thick electrode, it surged by 160% from 12.99 to 33.92 nm. These data along with the XPS analysis support our proposed mechanism that the negative feedback loop among reaction inhomogeneity, local lithium metal plating and subsequent SEI layer formation continuously increase the charge transfer resistance of the thick electrode, leading to the unusually fast capacity degradation.

2.4. Surface Protection to Break the Negative Feedback Loop in Thick Electrodes

In order to interrupt this detrimental cycle (**Figure 4a**), we attempted to protect the surface of the electrode to counter the repetitive degradation. We believed that the feedback loop of reduced reaction kinetics is strengthened because of the surface vulnerability to current hotspots and the corresponding side reactions that cause severe polarization. And, by reducing the surface side reaction, the linkage among the detrimental components can be weakened. In this regard, lithium phosphorous oxynitride (LiPON) was selected as a coating material functioning to serve as a stable artificial SEI layer^[76,77] (Figure 4b). Key criteria for selecting LiPON included i) high lithium diffusivity suitable for uniform lithium re-distribution

(Figure S9b, Supporting Information), and ii) chemical stability with lithium metal and electrolyte, enabling it to effectively isolate lithium from the electrolyte and suppress byproduct formation. We applied the LiPON coating to graphite electrodes using a magnetron sputtering method, achieving diverse coating thicknesses from 15 to 100 μm , while 50 μm coating yielded the most optimized performance (see Figure S9, Supporting Information for details). Figures S10 and S11 (Supporting Information) display the surface of the graphite electrode coated with 50 μm of LiPON, showing uniform coverage with the composition of P, O, and N elements corresponding to LiPON.

To verify the efficacy of the LiPON layer, we comparatively performed EIS testing, electrochemical cycling, and LIBS analysis for the thick electrodes with and without coating, as presented in Figure 4c-e. LiPON-coated graphite electrode demonstrated improved electrochemical performance, characterized by enhanced kinetics and reduced reaction inhomogeneity. Notably, as depicted in Figure 4c, the LiPON-coated electrode exhibited significantly lower overall resistance compared to the bare electrode after cycling. Particularly, the charge transfer resistance dropped to 22.5 Ω cm² compared to 71.3 Ω cm² for the uncoated electrode after repeated 50 cycles (See Figure S12, Supporting Information for Nyquist plot data). This level of resistance was even comparable to the 19.6 Ω cm² observed in the standard electrode (Figure 3a), indicating the successful surface protection. The lower resistance sustained could lead to the enhancement of the reaction homogeneity as shown in Figure 4d. According to LIBS analysis of the cycled electrodes, the heterogeneity of lithium along the electrode thickness was markedly suppressed. The plot shows that the amount of trapped lithium in the lower electrode regions could be reduced by approximately threefold compared with the uncoated graphite electrode. As a result of the enhanced kinetics and the reaction homogeneity, the cycle stability of the thick graphite electrode could be improved. The LiPON-coated electrode retained \approx 67% of its initial capacity, outperforming the uncoated thick electrode with $\approx 46\%$ retention after 50 cycles (Figure 4e). While further improvement should be made for the practical employment of this thick electrode configuration, these enhancements achieved through simple surface modification indicate that it is possible to overcome the difficulties inherent in thick electrodes by breaking one of the key links in the negative feedback loop. Furthermore, this approach suggests that, in addition to enhancing diffusion—conventional target for thick electrode optimization a comprehensive strategy addressing the surface reaction is essential for the successful implementation of high-loading electrodes.

3. Summary

In this study, we demonstrated that the rapid degradation of thick graphite electrodes originates from a negative feedback loop driven by depth-dependent lithium inhomogeneity and subsequent side reactions. Through comparative electrochemical testing and analysis, we proposed the following degradation process for thick electrodes: degradation begins with i) extended lithiumion diffusion paths within the electrode, leading to inhomogeneous reactions along the electrode depth. This inhomogeneity concentrates reactions at the electrode top layer, where ii) reaction

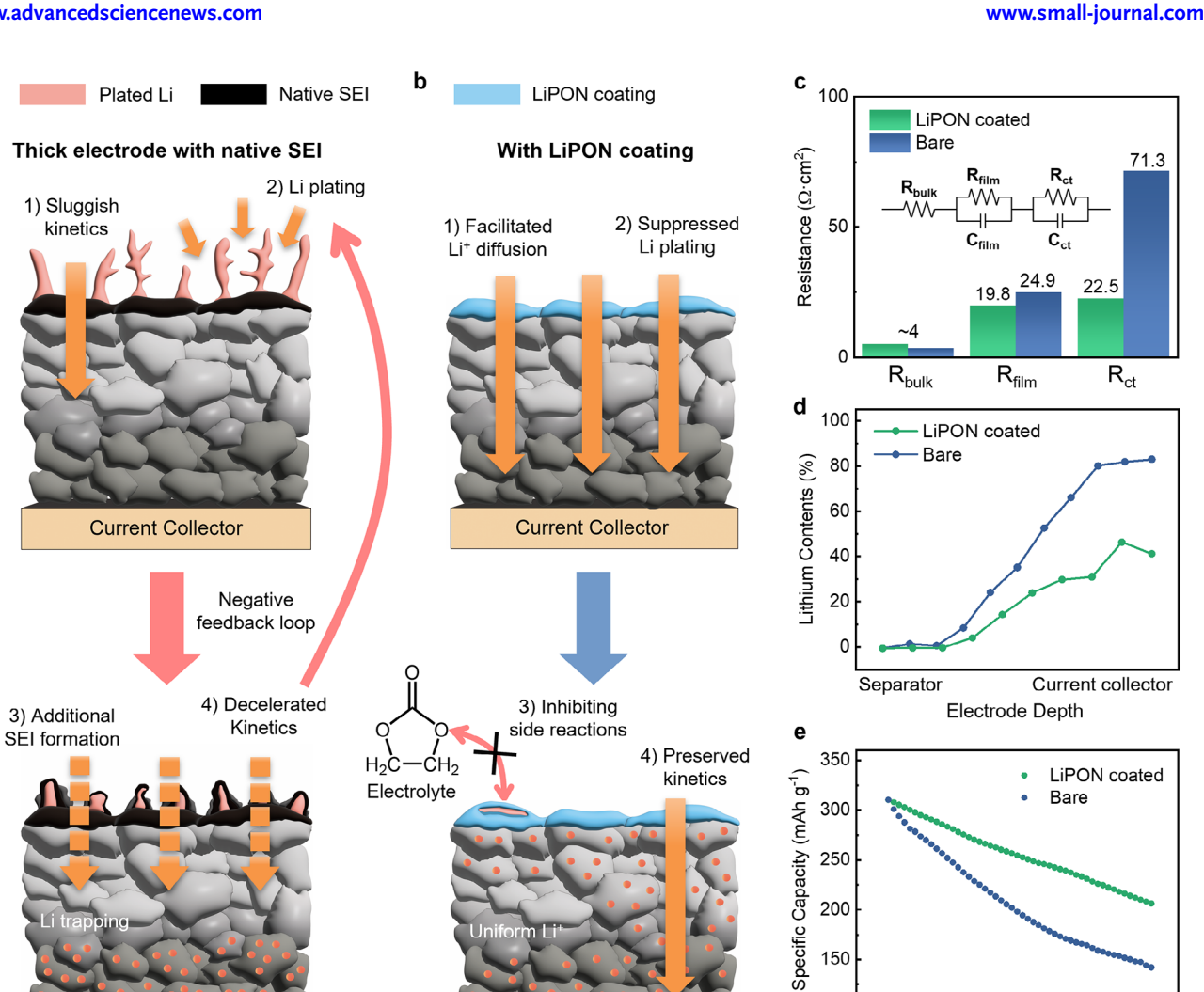


Figure 4. LiPON coating to break the negative feedback loop in graphite thick electrode. a) The degradation mechanism of graphite thick electrodes with red segments indicating plated lithium and yellow dots representing lithium ions. b) Effectiveness of the LiPON coating in mitigating the degradation processes. c) EIS result after 50 cycles and d) cycle life of bare (blue) and LiPON coated (green) thick electrode. e) Lithium content distribution along the electrode depth for bare (blue) and LiPON-coated (green) thick electrode.

Current Collector

byproducts accumulate, forming a surface layer. These byproducts then iii) impede the overall reaction kinetics, worsening inhomogeneity with each cycle and perpetuating a damaging cycle of reaction inhomogeneity and slowed kinetics, which accelerates electrode deterioration. To interrupt this negative feedback loop and mitigate related side reactions in high-loading graphite electrodes, we proposed a surface protection coating as a means to break the linkage among detrimental components. Although further improvements are necessary for practical application, cycle stability enhancements could be achieved through simple surface modification with LiPON. It suggests that overcoming the challenges of thick electrodes is possible by breaking a critical link in the negative feedback loop. Furthermore, it implies that, beyond improving diffusion—a common focus for optimizing thick electrodes—a comprehensive approach that also addresses surface reactions is essential for the successful implementation of high-loading electrodes.

Current Collector

4. Experimental Section

200 150 100

10

20

Cycle numbers

30

40

50

and-conditions) on Wiley Online Library for rules of use; OA articles are governed by the applicable Creative Commons

Electrochemical Measurements: The electrodes were fabricated by casting a slurry of active materials, carboxymethyl cellulose (CMC) and styrene-butadiene rubber (SBR) supplied by Samsung SDI were mixed in a weight ratio of 97.7:0.8:1.5 and added to deionized water on copper foil using doctor-blade method. The cast electrode was dried in a 70 °C vacuum oven overnight to dry out the deionized water solvent. The loading mass of the standard electrode was 10 mg cm⁻² and thick electrode was 15 mg cm⁻². These electrodes pressed by a roll-pressing machine to match the average loading density of the electrode was ≈ 1.4 mg cm⁻³. Coin-type cells (CR2032, Hohsen) were assembled by stacking a half-inch-diameter electrode, a slice of glass-fibre filter separator (grade GF/F filter, Whatman) and a lithium metal foil in an argon-filled glove box. The separator was soaked with electrolyte of 100 µL consisting of a 1.0 M solution of LiPF₆ in a mixture of ethyl carbonate and dimethyl carbonate (1:1 v/v, PanaX Etec). As additives, vinylene carbonate (VC) and fluoroethylene carbonate (FEC) were added at 2% and 5% by weight, respectively. Galvanostatic measurements of the charge/discharge of



www.small-journal.com

half-cell was performed in the voltage range of 0.005–1.6 V with a current density of 372 mA g $^{-1}$ (\approx 1C) at room temperature using a multichannel potentio-galvanostat (WBCS 3000, WonA Tech, Korea). A potentiostat (VSP-300, Bio-Logic Science Instruments) was used to measure the electrochemical impedance at room temperature in the frequency range of 10–3 MHz.

Material Characterizations—X-Ray Diffraction (XRD): X-ray diffraction patterns were obtained in the 2θ range of 10– 70° with a step size of 0.02° and step time of 2 s using an X-ray diffractometer (New D8 Advance, Bruker) equipped with Cu Kα radiation ($\lambda=1.54178$ Å). For XRD of rest samples, XRD was measured using an air-tight holder after disassembling the cell, and the samples were placed back in the glove box and the XRD measurement was repeated after 16 h.

Scanning Electron Microscopy (SEM): The morphology of the active materials was examined using scanning electron microscopy. SUPRA 55VP was installed at the National Instrumentation Center for Environmental Management (NICEM) at Seoul National University.

X-Ray Photoelectron Spectroscopy (XPS): The extent of electrolyte decomposition was determined using X-ray photoelectron spectroscopy (XPS; Sigma Probe, Thermo Fisher Scientific, U.K). When performing the etching process, 1 nm sputtering was performed at a time based on reference subastrate (Ta_2O_5), and etching was repeated a total of 49 times.

Cryogenic Transmission Electron Microscopy (Cryo-TEM): For preparation of sample for cryo-TEM analysis, cycled graphite powders were collected after electrochemical cycling and loaded on the Cu TEM grid (lacey carbon, 300 mesh) in Ar-filled glove box. TEM grids were put in a parafilm-sealed cryo grid box (Ted Pella, USA) and transferred to a cryo-transferstation filled with liquid nitrogen to prevent air exposure. Cryo-TEM experiments were performed on a JEOL JEM-2100F equipped with 1k × 1k Gatan UltraScan 1000 operated at 200 kV using the single tilt cryo-TEM holder (model 626, GATAN, USA).

Laser-Induced Breakdown Spectroscopy (LIBS): The state of charge (SOC) inhomogeneity was investigated using Laser-induced breakdown spectroscopy (LIBS) with a J200 system from Applied Spectra. In LIBS, a high-power laser is directed at the sample to convert it into a plasma state, allowing for elemental analysis. As the plasma returns to the ground state, it emits characteristic wavelengths of light unique to each element, enabling the identification and quantitative measurement of elements present in the material. For this study, a laser wavelength of 266 nm was used, with energies of 7.88 mJ for standard electrodes and 11.81 mJ for thicker electrodes. The cycled cells were disassembled immediately, and the electrodes were cleaned and quenched in liquid nitrogen to minimize the risk of lithium-ion redistribution within the electrode before the LIBS measurements were conducted. In the process of characterizing the electrode, the lithium intensity is quantified at each layer by progressively removing material from the electrode surface. Lithium content was measured for the delithiated electrode and lithium intensity measured from each layer is utilized to determine the lithium content based on a correlation established in a LIBS library (Figure \$13, Supporting Information), which links lithium intensity to lithium content in the graphite.

Magnetron Sputtering: Lithium phosphorous oxynitride (LiPON) films were deposited using reactive RF magnetron sputtering from a Li $_3$ PO $_4$ target in pure N $_2$. The Li $_3$ PO $_4$ target, provided by iTASCO company, had a diameter of 3 inches. Base pressure of the chamber was maintained at 10^{-7} mbar during the process, with a target-to-substrate distance of 5.3 cm. Sputtering power was set at 100 W, corresponding to a power density of 2.19 W cm $^{-2}$, and the N $_2$ pressure was held constant at 1.5×10^{-3} mbar. Under these optimized conditions, LiPON films of varying thicknesses ranging from 15 to 100 nm were produced by adjusting the sputtering time.

Supporting Information

Supporting Information is available from the Wiley Online Library or from the author.

Acknowledgements

This work was supported by the National Research Foundation of Korea (NRF) grant funded by the Korean government (MSIT) (No. RS-2023-00261543) and (NRF-2022M3I3A1082499). This work was also financially supported by the Samsung SDI and by the Hyundai Motor Chung Mong-Koo Foundation.

Conflict of Interest

The authors declare no conflict of interest.

Author Contributions

K.-H.K. and K.K. contributed equally to this work. K.-H.K., K.K., and K.K. conceived the original idea and designed the research project. K.-H.K. and K.K. carried out the structural and electrochemical characterizations of the materials; participated in all experiments and relevant analyses; and led the project direction. H.P. and J.P. performed the cryo-TEM measurements and provided constructive advice on the analysis of the TEM results. S.H. carried out deposition using sputtering equipment. K.-H.K., K.K., Y.K., and K.K. wrote the paper. K.K. supervised all aspects of this work.

Data Availability Statement

The data supporting this article have been included as part of the article and its Supplementary Information.

Keywords

degradation mechanism, electrode inhomogeneity, graphite anode, lithium-ion batteries, thick electrode

Received: November 13, 2024 Revised: January 10, 2025 Published online: March 23, 2025

- [1] M. Armand, J.-M. Tarascon, Nature 2008, 451, 652.
- [2] B. Dunn, H. Kamath, J.-M. Tarascon, Science 2011, 334, 928.
- [3] D. Bresser, K. Hosoi, D. Howell, H. Li, H. Zeisel, K. Amine, S. Passerini, J. Power Sources 2018, 382, 176.
- [4] J. Kim, Y. Kim, J. Yoo, G. Kwon, Y. Ko, K. Kang, Nat. Rev. Mater. 2023, 8. 54.
- [5] J. Liu, Z. Bao, Y. i. Cui, E. J. Dufek, J. B. Goodenough, P. Khalifah, Q. Li, B. Y. Liaw, P. Liu, A. Manthiram, Y. S. Meng, V. R. Subramanian, M. F. Toney, V. V. Viswanathan, M. S. Whittingham, J. Xiao, W. Xu, J. Yang, X.-Q. Yang, J.-G. Zhang, Nat. Energy 2019, 4, 180.
- [6] B. Liu, J.-G. Zhang, W. Xu, Joule 2018, 2, 833.
- [7] K. Kim, Y. Ko, O. Tamwattana, Y. Kim, J. Kim, J. Park, S. Han, Y.-R. Lee, K. Kang, Adv. Energy Mater. 2024, 14, 2304396.
- [8] M. T. McDowell, S. W. Lee, W. D. Nix, Y. Cui, Adv. Mater. 2013, 25, 4966.
- [9] B. Key, M. Morcrette, J.-M. Tarascon, C. P. Grey, J. Am. Chem. Soc. 2011, 133, 503.
- [10] C. K. Chan, H. Peng, G. Liu, K. McIlwrath, X. F. Zhang, R. A. Huggins, Y. Cui, Nat. Nanotechnol. 2008, 3, 31.
- [11] X. Chen, Y. Huang, J. Chen, X. Zhang, C. Li, H. Huang, Ceram. Int. 2015, 41, 8533.
- [12] M.-H. Park, M. G. Kim, J. Joo, K. Kim, J. Kim, S. Ahn, Y. Cui, J. Cho, Nano Lett. 2009, 9, 3844.



Finegan, A. Ouinn, D. S. Wragg, A. M. Colclasure, X. Lu. C. Tan.

- [13] H. Kim, B. Han, J. Choo, J. Cho, Angew. Chem., Int. Ed. 2008, 47, 10151.
- [14] M.-S. Shin, C.-K. Choi, M.-S. Park, S.-M. Lee, J. Electrochem. Sci. Technol. 2021, 13, 159.
- [15] D.-H. Kim, J.-H. Song, C.-H. Jung, D. Eum, B. Kim, S.-H. Hong, K. Kang, Adv. Energy Mater. 2022, 12, 2200136.
- [16] H. Park, H. Park, K. Song, S. H. Song, S. Kang, K.-H. Ko, D. Eum, Y. Jeon, J. Kim, W. M. Seong, H. Kim, J. Park, K. Kang, Nat. Chem. 2022, 14 614
- [17] W. M. Seong, K. H. Cho, J. W. Park, H. Park, D. Eum, M. H. Lee, I. S. Kim, J. Lim, K. Kang, Angew. Chem., Int. Ed. 2020, 59, 18662.
- [18] D. Eum, S.-O. Park, H.-Y. Jang, Y. Jeon, J.-H. Song, S. Han, K. Kim, K. Kang, Nat. Mater. 2024, 23, 1093.
- [19] H.-Y. Jang, D. Eum, J. Cho, J. Lim, Y. Lee, J.-H. Song, H. Park, B. Kim, D.-H. Kim, S.-P. Cho, S. Jo, J. H. Heo, S. Lee, J. Lim, K. Kang, *Nat. Commun.* 2024, 15, 1288.
- [20] D. Eum, H.-Y. Jang, B. Kim, J. Chung, D. Kim, S.-P. Cho, S. H. Song, S. Kang, S. Yu, S.-O. Park, J.-H. Song, H. Kim, O. Tamwattana, D.-H. Kim, J. Lim, K. Kang, *Energy Environ. Sci.* **2023**, *16*, 673.
- [21] S. J. Dillon, K. Sun, Curr. Opin. Solid State Mater. Sci. 2012, 16, 153.
- [22] K.-H. Choi, S.-J. Cho, S.-J. Chun, J. T. Yoo, C. K. Lee, W. Kim, Q. Wu, S.-B. Park, D.-H. Choi, S.-Y. Lee, S.-Y. Lee, Nano Lett. 2014, 14, 5677.
- [23] F. J. Günter, C. Burgstaller, F. Konwitschny, G. Reinhart, J. Electrochem. Soc. 2019, 166, A1709.
- [24] U. Plewnia, EV Engineering, https://www.evengineeringonline.com/ how-is-cell-to-pack-revolutionizing-ev-battery-pack-designs/>, June 2024.
- [25] J. T. Warner, The Handbook of Lithium-Ion Battery Pack Design: Chemistry, Components, Types, and Terminology, Elsevier, Amsterdam New York 2024.
- [26] G. Majeau-Bettez, T. R. Hawkins, A. H. Strømman, Environ. Sci. Technol. 2011, 45, 4548.
- [27] L. A.-W. Ellingsen, G. Majeau-Bettez, B. Singh, A. K. Srivastava, L. O. Valøen, A. H. Strømman, J. Indust. Ecol. 2014, 18, 113.
- [28] M. L. Carvalho, A. Temporelli, P. Girardi, Energies 2021, 14, 2047.
- [29] Y. Ye, L.-Y. Chou, Y. Liu, H. Wang, H. K. Lee, W. Huang, J. Wan, K. Liu, G. Zhou, Y. Yang, A. Yang, X. Xiao, X. Gao, D. T. Boyle, H. Chen, W. Zhang, S. C. Kim, Y. Cui, Nat. Energy 2020, 5, 786.
- [30] B. Tong, X. Li, Mater. Chem. Front. 2024, 8, 309.
- [31] M. Singh, J. Kaiser, H. Hahn, J. Electrochem. Soc. 2015, 162, A1196.
- [32] Y. Kuang, C. Chen, D. Kirsch, L. Hu, Adv. Energy Mater. 2019, 9, 1901457.
- [33] J. Sander, R. M. Erb, L. Li, A. Gurijala, Y.-M. Chiang, Nat. Energy 2016, 1, 16099.
- [34] K.-Y. Park, J.-W. Park, W. M. Seong, K. Yoon, T.-H. Hwang, K.-H. Ko, J.-H. Han, Y. Jaedong, K. Kang, J. Power Sources 2020, 468, 228369.
- [35] J. Billaud, F. Bouville, T. Magrini, C. Villevieille, A. R. Studart, Nat. Energy 2016, 1, 16097.
- [36] C. Huang, P. S. Grant, J. Mater. Chem. A 2018, 6, 14689.
- [37] R. Sommerville, P. Zhu, M. A. Rajaeifar, O. Heidrich, V. Goodship, E. Kendrick, Resour., Conser. Recycl. 2021, 165, 105219.
- [38] H. Zheng, J. Li, X. Song, G. Liu, V. S. Battaglia, Electrochim. Acta 2012, 71, 258.
- [39] Z. Du, D. L. Wood, C. Daniel, S. Kalnaus, J. Li, J. Appl. Electrochem. 2017, 47, 405.
- [40] K. Kitada, H. Murayama, K. Fukuda, H. Arai, Y. Uchimoto, Z. Ogumi, E. Matsubara, J. Power Sources 2016, 301, 11.
- [41] B.-S. Lee, Z. Wu, V. Petrova, X. Xing, H.-D. Lim, H. Liu, P. Liu, J. Electrochem. Soc. 2018, 165, A525.

- [42] D. P. Finegan, A. Quinn, D. S. Wragg, A. M. Colclasure, X. Lu, C. Tan, T. M. M. Heenan, R. Jervis, D. J. L. Brett, S. Das, T. Gao, D. A. Cogswell, M. Z. Bazant, M. D. Michiel, S. Checchia, P. R. Shearing, K. Smith, Energy Environ. Sci. 2020, 13, 2570.
- [43] C. Zhong, S. Weng, Z. Wang, C. Zhan, X. Wang, Nano Energy 2023, 117, 108894.
- [44] C. Sun, X. Ji, S. Weng, R. Li, X. Huang, C. Zhu, X. Xiao, T. Deng, L. Fan, L. Chen, X. Wang, C. Wang, X. Fan, Adv. Mater. 2022, 34, 2206020.
- [45] W. Huang, Y. Ye, H. Chen, R. A. Vilá, A. Xiang, H. Wang, F. Liu, Z. Yu, J. Xu, Z. Zhang, R. Xu, Y. Wu, L.-Y. Chou, H. Wang, J. Xu, D. T. Boyle, Y. Li, Y. Cui, Nat. Commun. 2022, 13, 7091.
- [46] G. Zhang, X. Wei, G. Han, H. Dai, J. Zhu, X. Wang, X. Tang, J. Ye, J. Power Sources 2021, 484, 229312.
- [47] X.-G. Yang, G. Zhang, S. Ge, C.-Y. Wang, Proc. Natl. Acad. Sci. USA 2018, 115, 7266.
- [48] U. R. Koleti, C. Zhang, R. Malik, T. Q. Dinh, J. Marco, J. Energy Storage 2019, 24, 100798.
- [49] B. Gyenes, D. Stevens, V. Chevrier, J. Dahn, J. Electrochem. Soc. 2014, 162. A278.
- [50] T. Deng, X. Zhou, J. Solid State Electrochem. 2016, 20, 2613.
- [51] M. Jo, S. Sim, J. Kim, P. Oh, Y. Son, Nanomaterials 2022, 12, 1956.
- [52] T.-H. Park, J.-S. Yeo, M.-H. Seo, J. Miyawaki, I. Mochida, S.-H. Yoon, Electrochim. Acta 2013, 93, 236.
- [53] J. Chong, S. Xun, H. Zheng, X. Song, G. Liu, P. Ridgway, J. Q. Wang, V. S. Battaglia, J. Power Sources 2011, 196, 7707.
- [54] J. U. Hwang, W. J. Ahn, J. S. Im, J. D. Lee, SN Appl. Sci. 2021, 3,
- [55] P. Smyrek, J. Pröll, H. Seifert, W. Pfleging, J. Electrochem. Soc. 2015,
- [56] K. O. Kim, S.-H. Park, H.-B. Chun, W. Y. Lee, B.-Y. Jang, D. Kim, J. H. Yu, K. S. Yun, J. Kim, O. L. Li, Y.-J. Han, ACS Appl. Mater. Interfaces 2023, 15, 36748.
- [57] T. H. L. Vuong, N. R. Mastoi, J. S. Nam, W. T. o. A. Ran, C. Ha, M.-S. Park, Y.-J. Kim, Chem. Eng. J. 2024, 497, 154534.
- [58] G. F. Dewald, S. Ohno, J. G. Hering, J. Janek, W. G. Zeier, Batteries Supercaps 2021, 4, 183.
- [59] M. Petzl, M. A. Danzer, J. Power Sources 2014, 254, 80.
- [60] J. Liu, Y. Zhang, J. Bai, L. Zhou, Z. Wang, Electrochim. Acta 2023, 454, 142362
- [61] Z. M. Konz, E. J. McShane, B. D. McCloskey, ACS Energy Lett. 2020, 5, 1750.
- [62] V. Kabra, R. Carter, M. Li, C. Fear, R. W. A. III, C. Love, P. P. Mukherjee, ACS Appl. Mater. Interfaces 2024, 16, 34830.
- [63] R. Carter, T. A. Kingston, R. W. Atkinson, M. Parmananda, M. Dubarry, C. Fear, P. P. Mukherjee, C. T. Love, Cell Rep. Phys. Sci. 2021, 2, 100351.
- [64] C. Fear, M. Parmananda, V. Kabra, R. Carter, C. T. Love, P. P. Mukherjee, Energy Storage Mater. 2021, 35, 500.
- [65] C. von Lüders, V. Zinth, S. V. Erhard, P. J. Osswald, M. Hofmann, R. Gilles, A. Jossen, J. Power Sources 2017, 342, 17.
- [66] P. J. Osswald, S. V. Erhard, A. Rheinfeld, B. Rieger, H. E. Hoster, A. Jossen, J. Power Sources 2016, 329, 546.
- [67] F. M. Kindermann, A. Noel, S. V. Erhard, A. Jossen, *Electrochim. Acta* 2015, 185, 107.
- [68] S. Zhang, G. Yang, S. Liu, X. Li, X. Wang, Z. Wang, L. Chen, Nano Energy 2020, 70, 104486.
- [69] J. S. Edge, S. O'Kane, R. Prosser, N. D. Kirkaldy, A. N. Patel, A. Hales, A. Ghosh, W. Ai, J. Chen, J. Yang, S. Li, M.-C. Pang, L. Bravo Diaz, A. Tomaszewska, M. W. Marzook, K. N. Radhakrishnan, H. Wang, Y. Patel, B. Wu, G. J. Offer, Phys. Chem. Chem. Phys. 2021, 23, 8200.
- [70] M. Su, Z. Wang, H. Guo, X. Li, S. Huang, W. Xiao, L. Gan, *Electrochim. Acta* 2014, 116, 230.
- [71] J. H. Sung, T. Kim, S. Kim, F. Hasan, S. K. Mohanty, M. K. Srinivasa, S. C. Reddy, H. D. Yoo, *Energies* 2023, 16, 6141.

16136829, 2025, 16, Downloaded from https://onlinelibrary.wiley.com/doi/10.1002/smll.202410795 by Korea Institute Of Science, Wiley Online Library on [01/06/2025]. See the Terms and Conditions

(https://onlinelibrary.wiley.com/terms-and-conditions) on Wiley Online Library for rules of use; OA articles are governed by the applicable Creative Commons License

www.advancedsciencenews.com

SCIENCE NEWS

www.small-journal.com

- [72] S. Li, Q. Meng, M. Fan, K. Yang, G. Tian, Ionics 2020, 26, 4443.
- [73] Q. Liu, A. M. Rao, X. Han, B. Lu, Adv. Sci. 2021, 8, 2003639.
- [74] H. Q. Pham, M. Mirolo, M. Tarik, M. El Kazzi, S. Trabesinger, Energy Storage Mater. 2020, 33, 216.
- [75] R. I. R. Blyth, H. Buqa, F. P. Netzer, M. G. Ramsey, J. O. Besenhard, P. Golob, M. Winter, Appl. Surf. Sci. 2000, 167, 99.
- [76] V. Lacivita, N. Artrith, G. Ceder, Chem. Mater. 2018, 30, 7077.
- [77] W. West, J. Whitacre, J. Lim, J. Power Sources 2004, 126, 134.

2410795 (10 of 10)